In Situ Observations of Phase Transitions in Metastable Nickel (Carbide)/Carbon Nanocomposites

Bernhard C. Bayer,[*,†,‡] David A. Bosworth,[§] F. Benjamin Michaelis,[†] Raoul Blume,[‖] Gerlinde Habler,[⊥] Rainer Abart,[⊥] Robert S. Weatherup,[†] Piran R. Kidambi,[†] Jeremy J. Baumberg,[∇] Axel Knop-Gericke,[#] Robert Schloegl,[#] Carsten Baehtz,[¶] Zoe H. Barber,[§] Jannik C. Meyer,[‡] and Stephan Hofmann[†]

[†]Department of Engineering, [§]Department of Materials Science and Metallurgy, and [∇]Cavendish Laboratory, University of Cambridge, Cambridge CB2 1TN, United Kingdom

[‡]Faculty of Physics and [⊥]Department of Lithospheric Research, University of Vienna, 1010 Vienna, Austria

[‖]Helmholtz-Zentrum Berlin für Materialien und Energie, 14109 Berlin, Germany

[#]Fritz-Haber-Institut der Max-Planck-Gesellschaft, 14195 Berlin, Germany

[¶]Institute of Radiation Physics, Helmholtz-Zentrum Dresden−Rossendorf, 01314 Dresden, Germany

S *Supporting Information*

ABSTRACT: Nanocomposite thin films comprised of metastable metal carbides in a carbon matrix have a wide variety of applications ranging from hard coatings to magnetics and energy storage and conversion. While their deposition using nonequilibrium techniques is established, the understanding of the dynamic evolution of such metastable nanocomposites under thermal equilibrium conditions at elevated temperatures during processing and during device operation remains limited. Here, we investigate sputter-deposited nanocomposites of metastable nickel carbide (Ni_3C) nanocrystals in an amorphous carbon (a-C) matrix *during* thermal postdeposition processing via complementary in situ X-ray diffractometry, in situ Raman spectroscopy, and in situ X-ray photoelectron spectroscopy. At low annealing temperatures (300 °C) we observe isothermal Ni_3C decomposition into face-centered-cubic Ni and amorphous carbon, however, without changes to the initial finely structured nanocomposite morphology. Only for higher temperatures (400−800 °C) Ni-catalyzed isothermal graphitization of the amorphous carbon matrix sets in, which we link to bulk-diffusion-mediated phase separation of the nanocomposite into coarser Ni and graphite grains. Upon natural cooling, only minimal precipitation of additional carbon from the Ni is observed, showing that even for highly carbon saturated systems precipitation upon cooling can be kinetically quenched. Our findings demonstrate that phase transformations of the filler and morphology modifications of the nanocomposite can be decoupled, which is advantageous from a manufacturing perspective. Our in situ study also identifies the high carbon content of the Ni filler crystallites at all stages of processing as the key hallmark feature of such metal−carbon nanocomposites that governs their entire thermal evolution. In a wider context, we also discuss our findings with regard to the much debated potential role of metastable Ni_3C as a catalyst phase in graphene and carbon nanotube growth.
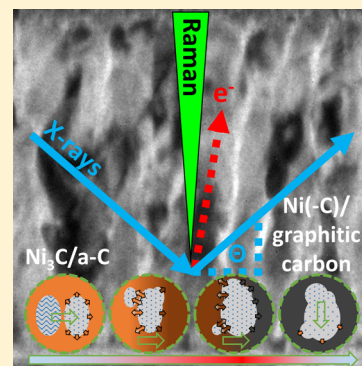
INTRODUCTION

Nanocomposite[1] thin films composed of metal and metal carbide nanoparticles in a carbon matrix have a wide application profile ranging from metallurgical hard coatings,[2,3] magnetics,[4,5] and sensing,[6,7] to energy storage and conversion.[8−10]

Substantial efforts in nonequilibrium deposition techniques,[11] such as sputter deposition, have enabled the controllable fabrication of nanocomposite thin films with thermodynamically *metastable* filler phases, such as metastable carbides (e.g., Ni_3C).[6,12−25] These metastable filler phases can provide novel functionalities and are hard to obtain in a scalable manner with other deposition techniques. Also bottom-up self-organized nanoscale structuring of filler and matrix phases has been realized.[26−30]

After the initial nonequilibrium deposition, metastable nanocomposite films are however commonly subjected to elevated temperatures during postdeposition treatments, device integration, and operation. The elevated temperatures can thereby enforce thermal equilibrium conditions onto the initially metastable structure of the nanocomposite. An understanding of the dynamic evolution of metastable nanocomposites under thermal equilibrium processing conditions remains however elusive.[6,12,13,28,31] This is due to only ex situ measurements being available to infer the mechanisms, while direct in situ characterization *during* the thermally induced phase evolution of the nanocomposites remains largely lacking. Such an understanding is however key to rationally engineer nanocomposites across their entire application spectrum.

To address this, we here employ complementary in situ characterization of nanocomposite thin films of nanostructured metastable[32−34] nickel carbide (Ni_3C) nanocrystals in an amorphous carbon (a-C) matrix[23] *during* thermal postdeposition processing via a combination of in situ X-ray diffractometry (XRD), in situ Raman spectroscopy, and in situ X-ray photoelectron spectroscopy (XPS). Ni−carbon nanocomposites are chosen as an archetypal model system for filler metals with a medium carbon affinity (i.e., metastable carbide formers),[11] a class of nanocomposites which further extends to other important materials combinations such as Co−carbon and Fe−carbon nanocomposites.[11,22,31] Our complementary in situ characterization thereby yields direct insights into the thermally induced phase evolution and dynamics in such metastable nanocomposite films.

We find that the room temperature deposited Ni_3C nanocrystals in the a-C matrix isothermally decompose already around ∼300 °C to face-centered-cubic (fcc) Ni nanocrystals, that are saturated with interstitially dissolved carbon (termed Ni(-C)), and amorphous carbon, which adds further carbon to the surrounding a-C matrix. In contrast to the low temperature of isothermal Ni_3C decomposition, we find that significant Ni-catalyzed graphitization of the amorphous carbon matrix during heating ramps and isothermal annealing only sets in at higher temperatures (∼400 °C and above), clearly confirming that Ni_3C decomposition and Ni-catalyzed graphitization are separate processes. Linked with the Ni-catalyzed graphitization, bulk-diffusion-mediated phase separation into coarse Ni and graphite grains also occurs only at higher temperatures. Thus, our findings demonstrate that filler phase transformations and nanocomposite morphology modifications can be decoupled, which is highly desirable from a manufacturing point of view. Upon natural cooling of the annealed nanocomposites, only minimal precipitation of deleterious additional carbon from the carbon saturated Ni crystallites is observed even for high temperature treatments. This implies that even for highly carbon saturated systems precipitation upon cooling can be kinetically quenched. Our findings demonstrate that the high carbon content of the Ni filler crystallites at all stages of processing is a hallmark feature of metal−carbon nanocomposites. Our study provides a framework for the optimization of film microstructure and functionality of metal (carbide)/carbon nanocomposites, which is crucial to their many envisaged applications.

In a wider context, our study also contributes to the elucidation of the recently debated role of Ni_3C as a possible intermediate bulk catalyst phase in Ni-catalyzed graphene[35−44] and carbon nanotube (CNT)[45−60] growth. Taking our Ni_3C/a-C nanocomposites as a model system for graphitization from Ni_3C, our in situ derived findings suggest that fcc Ni with interstitial carbon dissolved (Ni(-C)), rather than bulk Ni_3C, is the active catalyst phase during graphitic nanostructure growth under typical chemical vapor deposition (CVD) conditions.

■ METHODS

We deposit nanocomposite thin films (∼260 nm film thickness) of metastable Ni_3C nanoparticles in an a-C matrix in a two target (nickel, carbon) ionized magnetron sputter deposition system.[23,61,62] No intentional substrate heating is applied, leaving the employed sapphire substrates at temperatures less than 120 °C (maximum temperature due to plasma heating). To induce deposition of the metastable Ni_3C phase, a negative bias of −150 V is applied to the substrate holder

during deposition.[23] The composition of the films obtained is ∼70 atom % C and ∼30 atom % Ni. Following deposition and sample transport in air, the as-deposited Ni_3C/a-C films are subjected to annealing treatments up to 800 °C in a vacuum (∼10^{-5} mbar) while concurrently measuring in situ X-ray diffraction (XRD, X-ray wavelength 0.1078 nm), in situ Raman spectroscopy (excitation wavelength 532 nm), and in situ X-ray photoelectron spectroscopy (XPS). Subsequently samples are left to cool naturally (∼100 °C/min initial cooling rate) to room temperature (RT). Complementary ex situ characterization is performed using cross-sectional transmission electron microscopy (TEM), selected area electron diffraction (SAED),[63] and plan-view scanning electron microscopy (SEM) as well as ex situ XRD and Raman spectroscopy. Further details of the experimental methods are included in the Supporting Information.

We note that it is notoriously difficult to assign the carbon-containing Ni_3C (space group $R\bar{3}c$) with certainty when there is the possibility of the largely isostructural carbon-free hexagonally closed packed (hcp) Ni phase (space group $P6_3/mmc$) also being present.[24,64−66] This difficulty arises since both phases consist of an hcp Ni (sub)lattice, which in the case of Ni_3C has an ordered sublattice of interstitial carbon added.[64] The additional ordered interstitial carbon does however only slightly change the resulting diffraction patterns, which is why SAED and XRD routinely exhibit difficulties in assigning either phase with certainty.[24,64,65] This picture is further complicated since recent reports[24,64] suggested the formation of carbon-containing hcp Ni (termed hcp NiC_y) which differs from Ni_3C only in terms of decreased interstitial carbon ordering; i.e., hcp NiC_y is a disordered form of Ni_3C. We discuss details of our phase assignment to Ni_3C in the Supporting Information. We note however that our general usage of the terms nickel carbide and Ni_3C in this study not only includes fully ordered Ni_3C but also encompasses disordered forms of Ni_3C, approaching the recently suggested[24,64] hcp NiC_y form (i.e., hcp Ni sublattice including disordered interstitial carbon).

■ RESULTS

We start by describing the structure and morphology of the films throughout the thermal processing based on ex situ characterization and then link this to the dedicated in situ experimentation in order to reveal the mechanisms and dynamics of the underlying processes.

Ex Situ Characterization. Figure 1a shows ex situ TEM bright field images of cross sections of the Ni_3C/a-C films in their as-deposited state, and after annealing at 300 and 800 °C, alongside the corresponding SAED patterns in Figure 1b. The corresponding plan-view SEM images and Raman spectra are presented in Figure 2a and 2b, respectively. The samples were annealed in a vacuum by global heating on a resistive heater.

Figure 1a shows that the as-deposited films exhibit a columnar grain structure with dark contrast grains that are elongated perpendicular to the substrate surface (average grain sizes: long axis perpendicular to substrate surface, 88 ± 44 nm; short axis parallel to substrate surface, 20 ± 8 nm) and that are embedded in a matrix of lighter contrast, which is finely dispersed between the dark contrast grains. On the basis of the SAED, we identify the dark contrast grains as Ni_3C (reflections indexed in Figure 1b, see also Supporting Information for discussion of Ni_3C assignment)[24,64−66] and the finely dispersed light contrast matrix as a-C (based on the absence of a strong graphitic reflection in the SAED in Figure 1b). The top surface

Figure 1. (a) Cross-sectional bright field TEM micrographs of Ni−carbon nanocomposites in as-deposited state (bottom) and after anneals at 300 (middle) and 800 °C (top). (b) SAED patterns corresponding to (a). The overlays show extracted radially integrated SAED profiles[63] with the identified phases indexed. Note that in the SAED pattern of the as-deposited film additional possible Ni$_3$C(104) reflections[24,64,65] are indicated (see Supporting Information for a comment on Ni$_3$C phase assignment). Estimated uncertainty in temperature for the ex situ anneals is ±10 °C.

Figure 2. (a) SEM micrographs (plan view) of the Ni−carbon nanocomposite surface in as-deposited state (bottom) and after anneals at 300 (middle) and 800 °C (top), corresponding to Figure 1. (b) Ex situ Raman spectra of Ni−carbon nanocomposites in as-deposited state (bottom) and after anneals at 300 (middle) and 800 °C (top), corresponding to (a) and Figure 1. The intensities of the as-deposited and 300 °C spectra have been multiplied by the indicated values to improve readability.

of the as-deposited films appears smooth in the TEM cross section which aligns well with the largely featureless SEM image in plan view (Figure 2a). In keeping with our indirect SAED assignment of the matrix to a-C, the Raman spectrum in Figure 2b shows a very low intensity peak representing a merged D and G band and no signal in the 2D region, both indicative of highly disordered carbon.[67]

Upon annealing at 300 °C and subsequent cooling in the vacuum the cross-sectional grain structure of columnar metal-containing grains in a finely dispersed amorphous carbon matrix is preserved (Figure 1a). Only some increase in the average dark contrast grain size perpendicular to the substrate occurs (long axis perpendicular to substrate, 105 ± 63 nm; short axis parallel to substrate, 29 ± 10 nm), indicating that dark contrast grains start to merge in the direction perpendicular to the substrate. Likewise, only very limited roughening of the film surface (Figure 2a) is observed. While the overall change in film morphology is limited, the corresponding SAED pattern indicates a drastic change in the dark contrast Ni-containing phase from Ni$_3$C to fcc Ni (Figure 1b). Concurrently, we find only a small increase in the carbon ordering, indicated by the only small increase in overall Raman intensity and the still strongly overlapping D and G peaks as well as the lack of a 2D peak (Figure 2b).[20,67] Correspondingly, in the SAED (Figure 1b) a pronounced graphitic peak remains absent for the 300 °C annealed films, confirming a still largely amorphous carbon matrix.

Further annealing at 800 °C (and subsequent cooling) leads to a drastic change in film morphology. TEM (Figure 1a) and SAED (Figure 1b) show that pronounced phase separation into coarse and more isotropically shaped dark contrast metallic fcc Ni grains (isometric grain size, 83 ± 42 nm) and coarse carbon grains (isometric grain size, 60 ± 33 nm) occurs. The as-deposited columnar grain structure of fine-grained metallic filler and interdispersed a-C matrix is thereby destroyed. The appearance of a strong graphitic reflection in SAED (Figure 1b) indicates that significant ordering of the carbon toward a graphitic structure has occurred. A graphitic interlayer distance of ∼0.35 nm is estimated from the SAED pattern, which is consistent with nanocrystalline graphite with partly turbostratic layer stacking. From the cross-sectional TEM we further find that graphitic domains form largely toward the top surface of the film. This corresponds well with the dark contrast patches apparent in SEM which we ascribe to graphitic grains (Figure 2a). The graphitization is also well reflected in the corresponding Raman spectrum (Figure 2b) which for the 800 °C sample shows intense and well-separated D and G peaks, as well as the appearance of a 2D signal. This confirms the formation of nanocrystalline graphite,[31,67,68] where we estimate from the ratio of the D to G peak intensities a lower bound for the in-plane-ordering size of ∼6.5 nm.[67] The drastic change in structure *and* morphology of the nanocomposite indicates that significant bulk diffusion has occurred in the Ni−carbon system during the high temperature annealing.

Our ex situ observations so far indicate three major processes that occur upon the heat treatments: (1) At 300 °C the filler phase transforms from Ni$_3$C to fcc Ni. (2) At annealing temperatures greater than 300 °C the graphitization of a-C to nanocrystalline graphite sets in. (3) Ni grain growth and thus destruction of the fine-grained nanocomposite morphology occurs. While graphitization and Ni grain growth appear linked, the Ni$_3$C decomposition (to fcc Ni and a-C) at 300 °C did not influence the fine-grained morphology of the as-deposited nanocomposite. This indicates that phase transformations and film morphology modifications can be decoupled in such nanocomposite systems.

The ex situ characterization in Figures 1 and 2 is however limited to the "cold" postprocessing state of the nanocomposites, and thus cannot directly elucidate the state of the material while the phase transformations and morphology

changes are actually occurring at elevated temperature. Therefore, important aspects such as whether the phase transformations proceed during heating ramps, isothermally at temperature, or are a result of subsequent cooling remain unknown.[6,69−75] Also, ex situ characterization can only indirectly imply the temperature regimes and time scales over which the observed processes proceed. To reveal such dynamics, we now link our ex situ observations above to dedicated in situ characterization.

In Situ XRD. We first investigate the structural evolution of the Ni_3C/a-C nanocomposites using a previously described in situ XRD system,[76−79] in which the Ni_3C/a-C nanocomposite samples are globally heated by a resistive heater (as in our ex situ annealing above). Figure 3a shows a series of in situ X-ray diffractograms acquired at salient stages during the vacuum annealing of an as-deposited Ni_3C/a-C nanocomposite. As deposited we find a diffraction pattern corresponding to essentially phase pure Ni_3C (see also Supporting Information for a comment on assignment/definition of Ni_3C).[24,64−66] With heating this pattern transforms to show the reflections of fcc Ni. We extract the corresponding phase fractions of Ni_3C and fcc Ni by Rietveld refinement and plot the evolution of the phase fraction in Figure 3b. In agreement with our ex situ observations above, we find the onset of the $Ni_3C \rightarrow$ fcc Ni transformation at 300 °C. The inset in Figure 3b shows how this phase transformation proceeds with time, indicating a phase transformation from Ni_3C to fcc Ni over a time scale of tens of minutes at 300 °C. Upon further annealing to temperatures higher than 300 °C and up to 800 °C, the fcc Ni remains the only observed phase. Also after natural cooling from 800 °C to room temperature, fcc Ni remains the only detected phase. After cooling we find from Rietveld refinement that the fcc Ni lattice constant is 0.35255 ± 0.00005 nm, which corresponds[32] to a carbon content of 0.19 ± 0.07 atom % in the Ni. This carbon content is significantly higher than the equilibrium carbon content expected for Ni at room temperature of <0.01 atom %[32,80] and instead corresponds to the expected equilibrium carbon content in Ni for temperatures between 580 and 690 °C.[80] This observation thus indicates that the cooled fcc Ni particles still contain a relatively large amount of carbon interstitially dissolved within them; i.e., the Ni particles are a solid solution of carbon interstitially dissolved in fcc Ni (here termed Ni(-C)).

We note that we do not observe the appearance of any Bragg peak associated with graphite in the XRD data (neither during annealing nor upon natural cooling). In contrast, for the same processing temperatures the ex situ analysis clearly shows the formation of nanocrystalline graphitic grains via SAED (Figure 1b) and Raman spectroscopy (Figure 2b). SAED and Raman spectroscopy are known to be more sensitive toward the presence of smaller ordered graphitic regions compared to XRD, which is only sensitive to larger ordered regions.[6,81] Therefore, the lack of a graphitic signal in XRD ("XRD-amorphous" structure of carbon matrix; also confirmed by ex situ XRD of the same ex situ 800 °C annealed sample from Figures 1 and 2) reaffirms that the carbon matrix is composed of small nanometer-sized grains even after 800 °C annealing. Due to this XRD-amorphous nature of the nanocrystalline graphite, our in situ XRD measurements cannot, however, answer the important question of whether the formation of the nanocrystalline graphite occurs during the initial heating ramp, isothermally, or upon cooling. All these scenarios have been previously suggested in the literature as possible graphite
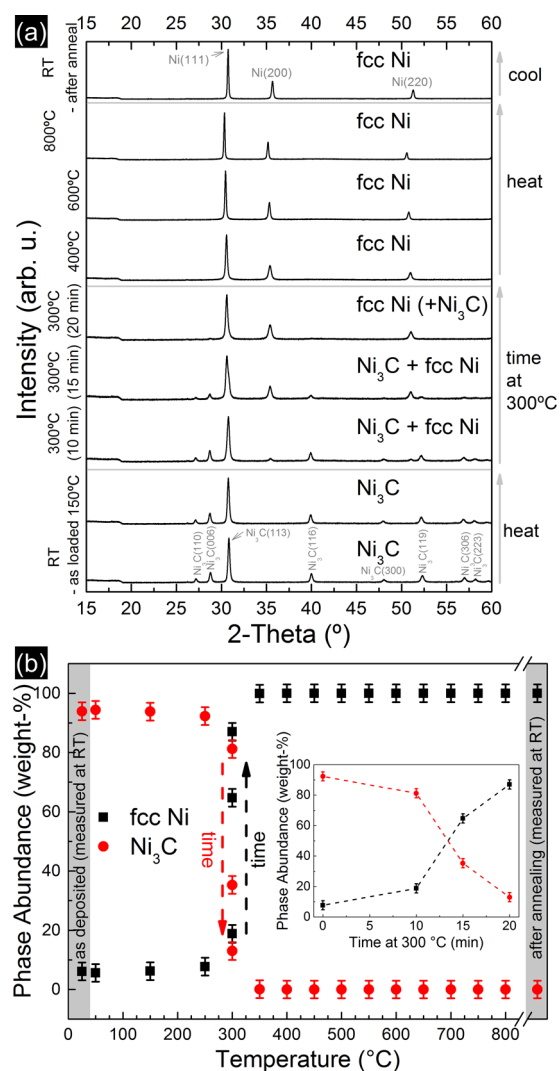
Figure 3. (a) In situ XRD patterns (X-ray wavelength 0.1078 nm) showing temperature and time-resolved evolution of the structure of the Ni−carbon nanocomposites (from bottom to top). The step at ~18° is related to the arrangement of detector and X-ray entrance/exit slits into the reaction chamber. The small peak at 26.2° is related to the sapphire substrate. We note that reflection positions shift throughout temperature dependent scans due to thermal expansion. (b) Phase abundance of Ni_3C and fcc Ni as a function of annealing temperature, extracted from the in situ data in (a) via Rietveld refinement. Only Ni and Ni_3C were included in the abundance quantification, while graphite was not detectable in the XRD data (see main text) and therefore not included in the abundance estimation. The inset shows the evolution of the phase abundance of Ni_3C and fcc Ni as a function of annealing time at 300 °C. Note that based on qualitative phase identification fcc Ni is absent for as-deposited films and annealed films up to 250 °C. As an upper bound of fcc Ni content that could be "hidden" in the signal noise, quantitative Rietveld refinement indicates a maximum of <7 wt %. Estimated uncertainty in temperature for the in situ XRD measurements is ±40 °C.

formation pathways for Ni−carbon systems.[6,69−75] To clarify this point, we now turn to in situ Raman spectroscopy in Figure 4, which provides higher sensitivity toward smaller scale carbon ordering during the thermal processing.

In Situ Raman Spectroscopy. We use a previously described in situ Raman spectroscopy setup[82,83] in which the Raman probe laser (532 nm) is simultaneously used for highly localized sample heating and sensing (optical spot size ~1 μm).
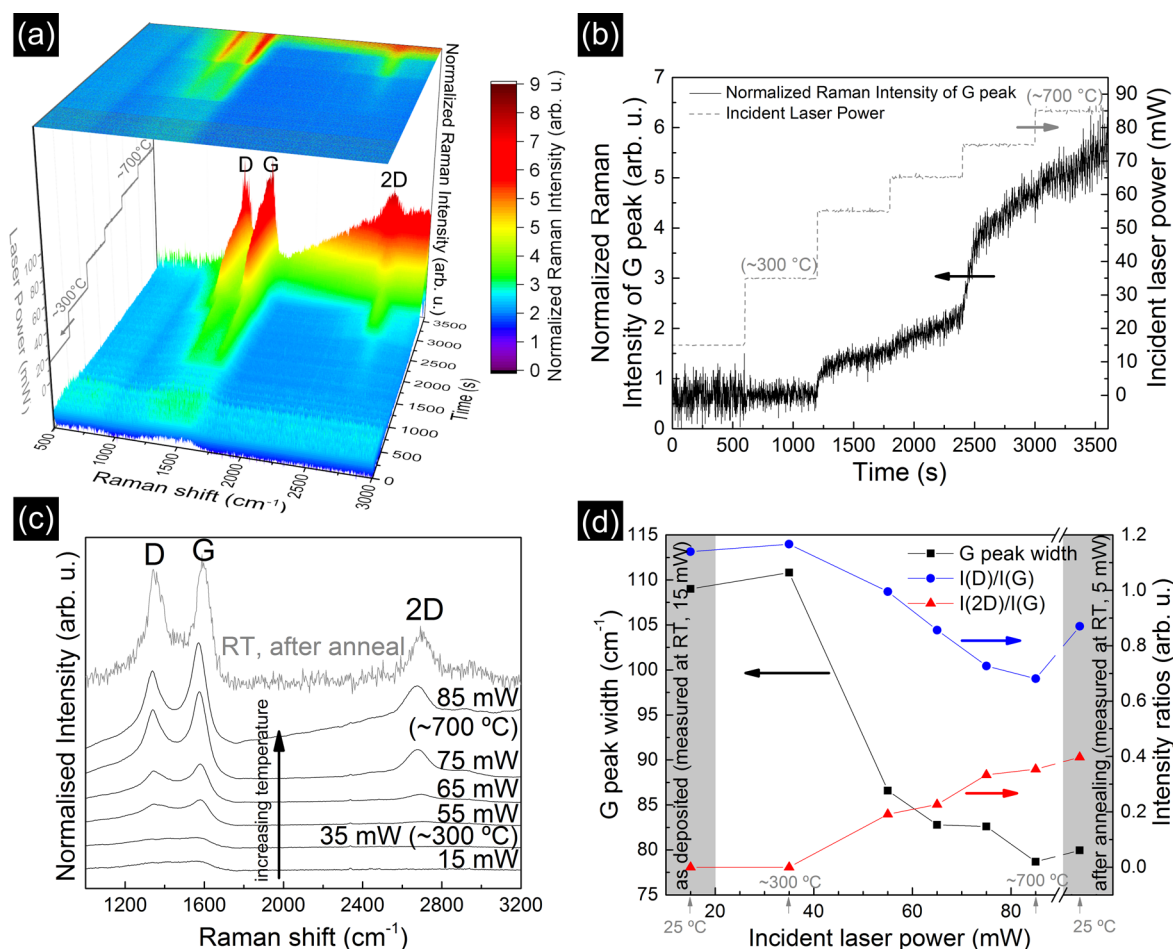
Figure 4. (a) Typical in situ Raman spectroscopy data set showing the evolution of the carbon-related Raman bands as a function of stepwise increases in incident laser power (normalized Raman intensity false-colored surface map with x-axis showing Raman shift, y-axis showing time, and z-axis showing normalized Raman intensity; an additional false-colored surface projection of normalized Raman intensity is projected onto the xy-plane [top of graph]; the yz-plane shows the stepwise increased incident laser power as a function of time). (b) Time evolution of the normalized G peak intensity (extracted from (a)) as a function of the stepwise increases in incident laser power. (c) Time-averaged Raman spectra as a function of applied laser power. Averaging was performed over the time-resolved Raman spectra in (a) at constant incident laser power steps. Spectra are offset for clarity. (d) G peak width and $I(D)/I(G)$ and $I(2D)/I(G)$ intensity ratios as a function of applied laser power, extracted from the Raman spectra in (c). For a comment on temperature estimations, see the Supporting Information. Estimated uncertainty in temperature for the in situ Raman measurements is ±50 °C.

Figure 4a shows the data from a typical in situ experiment where the laser power is increased stepwise while measuring time-resolved Raman spectra at a fixed position on the Ni−carbon nanocomposite film. Note that in this setup with increasing laser power not only the temperature of the sampled area but also the intensity of the acquired Raman spectra increases. In order to remove this influence of increasing signal intensity related to increased laser power, only the *normalized* Raman intensity is plotted here, where the measured Raman raw intensity has been divided by the incident laser power.

We estimate the local temperature from the in situ laser heating via calibration against ex situ annealed samples (see Supporting Information): For a laser power of 15 mW, heating of the sample is found to be negligible. Temperatures of ~300 °C for 35 mW and of ~700 °C for 85 mW are estimated, respectively, with a linear relationship between temperature and applied laser power.[83,84] We note that at higher laser powers of >75 mW the background in the spectra also develops a contribution due to thermal blackbody radiation,[85] although we find that the blackbody signal is insufficient in intensity to reliably estimate local temperatures from it.

Figure 4a shows that, in agreement with our ex situ data, the as-deposited nanocomposite film initially shows a low intensity, merged D and G band and no 2D signal, consistent with the initially present a-C.[67] When increasing the laser power (and thus local heating temperature) we find that gradually the D and G bands become more intense and narrower and their overlap reduces. Concurrently, a 2D signal emerges (starting at 55 mW). This is consistent with graphitization in the sample from a-C toward nanocrystalline graphite.[67]

To quantify the temporal dynamics of this process, Figure 4b follows the time evolution of the G peak intensity ($I(G)$) as a function of the stepwise increases in laser heating. For laser powers of up to 35 mW (~300 °C) we find a roughly constant $I(G)$ with time. This confirms that graphitic ordering for anneals up to 300 °C is minor. Increasing the laser power from 35 to 55 mW (corresponding to ~470 °C) results in an immediate sharp increase in $I(G)$ followed by a continuous gradual increase in $I(G)$ with time. These observations imply that graphitization occurs during the initial rapid heating ramp and then further continues isothermally. We find similarly sharp increases in $I(G)$ with stepwise laser power increases, followed

by a gradual increase in $I(G)$ with time, also for other power steps up to 85 mW. The variation in magnitude of these sharp $I(G)$ increases for different laser powers may relate to the Ni–carbon system crossing activation energy thresholds during particular power steps (e.g., the step from 35 (~300 °C) to 55 mW (~470 °C) may be related to a completed transition from Ni_3C to fcc Ni). We emphasize that (unlike the ex situ measurements above) these Raman measurements are taken in situ *on the hot sample*, i.e. without any intermediate cooling. Therefore, the observed evolution of the Raman signature from a-C toward nanocrystalline graphite *during* annealing clearly confirms that in these nanocomposites graphitization occurs during heating ramps and isothermal annealing, rather than solely by precipitation on cooling.

Figure 4c plots time-averaged spectra for each laser power (i.e., averaging over the isothermal increase in signal), which improves the signal-to-noise ratio. Extracted from these averaged spectra, we quantify the G peak width, and the intensity ratios of $I(D)/I(G)$ and $I(2D)/I(G)$ as a function of incident laser power in Figure 4d. This confirms that with increasing temperature the G peak generally narrows and the $I(2D)/I(G)$ ratio increases while the $I(D)/I(G)$ ratio concurrently decreases, again consistent with graphitization from a-C toward nanocrystalline graphite.[67]

Upon cooling (i.e., after the laser power is reduced from 85 to 5 mW) we find an only a minor increase (<10%) in the G peak normalized intensity $I(G)$ as well as an increase in the $I(D)/I(G)$ ratio. This indicates that at most only a small amount of disordered carbon can have precipitated out of the Ni particles upon cooling, directed toward the buried Ni filler/carbon matrix interface and/or toward the sample surface. To further elucidate such changes on the nanocomposite's (sub)surface, we finally employ in situ XPS.

In Situ XPS. XPS provides (sub)surface sensitive chemical information (total information depth at the applied excitation energy is estimated to ~3.6 nm), which is complementary to the "bulk"-sensitive XRD (estimated information depth of ~200 nm) and Raman spectroscopy (information depth for such nanocomposite films typically estimated at ~100 nm[81]). Figure 5 shows in situ XP spectra of the C 1s (Figure 5a) and Ni 2p (Figure 5b) core level evolution of a Ni_3C/a-C nanocomposite film during salient stages of vacuum annealing, where global back-side heating is used in the in situ XPS chamber,[86,87] similar to our ex situ preparations and the in situ XRD. We first assign the observed XPS peaks based on comparison to literature (see also Supporting Information Table 1) before describing the observed evolution of surface chemistry upon annealing.

The C 1s spectrum of the as-loaded film (i.e., as-deposited film after air exposure prior to XPS measurements) has a majority component at a binding energy (BE) of 284.9 eV, which we assign to disordered carbon (with a certain fraction of sp^3-like bonding)[88,89] followed by a lower intensity component at 284.4 eV which we attribute to sp^2 bonded carbon.[88,89] A minor component is at 283.7 eV, which has been previously ascribed to a solid solution of carbon interstitially dissolved in metallic Ni[88] (here termed Ni(-C)), where the comparably high BE indicates significant carbon dissolution) but also to Ni_3C.[90] The reported BEs of Ni_3C however vary in the literature: Notably another minority component in our C 1s data lies at a very low BE of 283.0 eV, which also has been previously assigned to crystalline Ni_3C.[19] (We note that the monolayer thin carbide Ni_2C surface reconstruction on Ni(111) has also
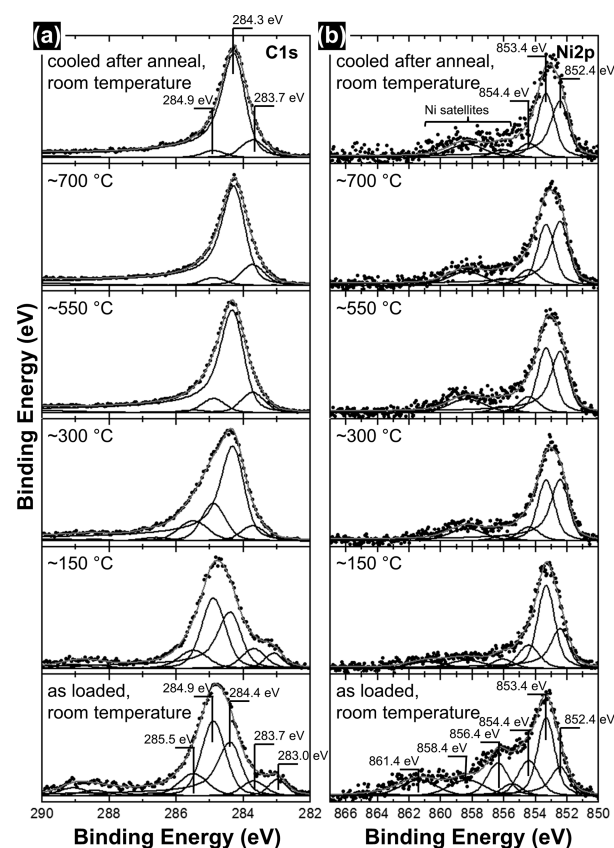
Figure 5. In situ XP spectra of the (a) C 1s and (b) Ni 2p regions as a function of vacuum annealing temperature (from bottom to top). Estimated uncertainty in temperature for the in situ XPS measurements is ±40 °C.

been reported but at a slightly higher binding energy of 283.2 eV.[91]) We find that the presence of this low energy peak at 283.0 eV correlates well with the presence of crystalline Ni_3C signatures in TEM/SAED and XRD data of our as-deposited films and upon heating (see below). At higher BEs one further C 1s minority component in the as-deposited films is located at 285.5 eV, which is a signature of adventitious carbon adsorbates from sample storage in ambient air.[92,93]

The corresponding Ni 2p spectrum of the as-loaded film shows peaks corresponding to an oxidized Ni surface (minor component at 854.4 eV and peaks with BE > 855 eV in Ni 2p),[94] which is consistent with the sample having been stored in ambient air prior to loading into the in situ XPS system.[19] The nonoxide majority Ni 2p component in the as-loaded films is at 853.4 eV, which is close to literature assignments of Ni with carbon interstitially dissolved (Ni(-C))[88] but is also consistent with previously reported BEs for Ni_3C.[21,22,90] Another smaller Ni 2p component in the as-loaded sample is at 852.4 eV, which is commonly attributed to metallic Ni.[88]

Based on our assignments, we conclude that the as-loaded sample surface exhibits signs of Ni_3C (C 1s, 283.0 eV, and/or 283.7 eV/Ni 2p, 853.4 eV) and a substoichiometric Ni(-C) solid solution (283.7 eV/853.4 eV). A combination of these C 1s signatures is commonly found for XP spectra of Ni_3C/a-C nanocomposites, even when only Ni_3C crystals are observed in TEM/SAED or XRD (as is also the case here).[19] A mixture of disordered sp^3-like (284.9 eV) and sp^2 (284.4 eV) carbon is further found in the as-loaded samples, which is consistent with the a-C matrix observed in TEM/SAED and Raman spectros-
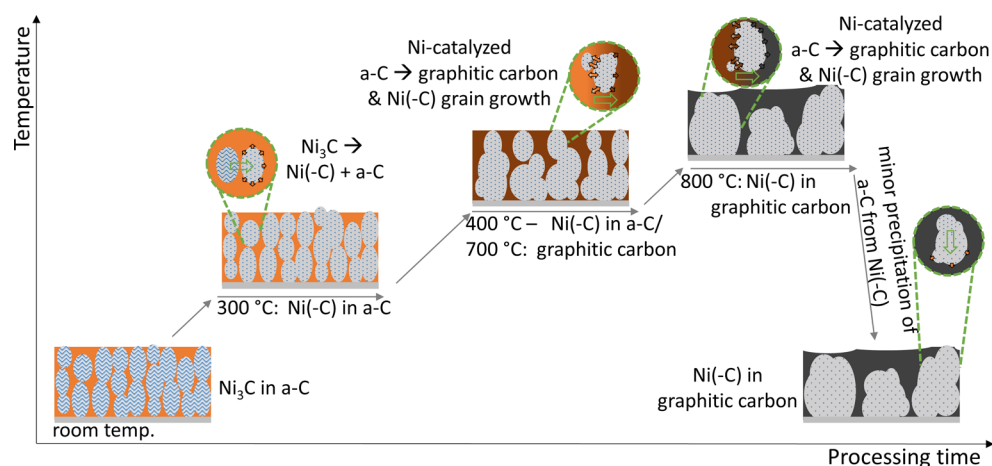
Figure 6. Schematic sketch illustrating the morphological and structural evolution of the Ni−carbon nanocomposites during thermal annealing, as derived from our in situ study.

copy. The as-loaded spectra further indicate that upon sample storage in air surface oxidation has occurred. This presumably proceeds via the decomposition of an initially present Ni$_3$C surface, resulting in an mixture of some oxidized Ni (854.4 eV and >855 eV), some metallic Ni (852.4 eV), and some of the observed a-C.[95] Adventitious carbon adsorption (285.5 eV) onto the sample surface from storage in ambient air further complicates the surface chemistry in the as-loaded sample.

We now turn to the thermal evolution of the surface chemistry upon vacuum annealing: When heating to 150 °C, the Ni oxides reduce (decrease of 854.4 eV and >855 eV components) and a corresponding small increase in metallic Ni is observed (852.4 eV). The Ni 2p now predominantly shows the presence of Ni$_3$C/Ni(−C) (853.4 eV) accompanied by a small amount of metallic Ni (852.4 eV). The C 1s signatures do not show significant changes when heating from room temperature to 150 °C.

Increasing the annealing temperature further to 300 °C (which is the Ni$_3$C decomposition temperature estimated from in situ XRD and TEM above) leads however to a drastic change in both the Ni 2p and C 1s signatures: The Ni$_3$C/Ni(−C) component in the Ni 2p (853.4 eV) significantly reduces in relative intensity (but does not vanish), while the metallic Ni component (852.4 eV) increases, yielding now roughly a 1:1 ratio of Ni$_3$C/Ni(−C) and metallic Ni intensities. Importantly, the 283.0 eV component in the C 1s concurrently disappears, suggesting that Ni$_3$C decomposes. The in situ XPS data therefore corroborates isothermal decomposition of Ni$_3$C (reduction of 853.4 eV Ni 2p and vanishing 283.0 eV C 1s) and suggests that this decomposition results in a mixture of metallic Ni (increasing 852.4 eV Ni 2p) and Ni that still has a significant fraction of carbon interstitially dissolved (Ni(-C), nonvanishing intensity at 853.4 eV in Ni 2p and 283.7 eV in C 1s). Concomitantly, the disordered sp^3-like carbon component (284.9 eV which was the predominant C 1s signal in the as-loaded sample) reduces in relative intensity while the sp^2 component (284.4 eV) increases and becomes the new majority component. This is a first sign of graphitization.[89] This XPS result at 300 °C implies a lower onset temperature of graphitization compared to the Raman data in Figure 4 above. XPS is however more sensitive to changes in local bonding environments (e.g., small disconnected regions transitioning from disordered carbon to sp^2) while being less sensitive to the spatial extents of this bonding. In contrast, Raman spectroscopy

is more suitable for probing the contiguous nature, i.e. crystallite size, of the bonded carbon.[96] Therefore, the combination of in situ XPS and in situ Raman spectroscopy indicates that at 300 °C a transition of disordered carbon to sp^2 bonding starts, but that the spatial extents of the formed sp^2 regions remain very small.

Upon further increasing the annealing temperature to 550 °C and then 700 °C, a further reduction of the disordered carbon component and increase of the sp^2 component in the C 1s is consistent with the emergence and growth of the 2D Raman peak and the corresponding decrease in $I(D)/I(G)$ ratio (Figure 4d). This shows that in this higher annealing temperature region (550 °C and above) spatially extended sp^2-bonded graphitic regions are isothermally formed. (Further note that from 300 to 550 °C the 285.5 eV component also disappears, which is indicative of the removal of adventitious carbon contamination. A minor residual Ni oxide component at 854.4 eV remains throughout the experiment.) In contrast to the clear signs of graphitization observed in the C 1s, the Ni 2p fingerprint does not show significant further evolution with increasing temperatures from 300 to 700 °C, implying that the chemical state of the mixture of metallic Ni and a Ni(−C) solid solution on the sample (sub)surface remains largely unchanged for annealing temperatures greater than 300 °C.

Upon natural cooling in the vacuum neither the C 1s nor the Ni 2p fingerprint changes significantly. In particular, the intensity of the C 1s peak immediately after cooling is not higher than the C 1s intensity at 700 °C immediately before cooling. This indicates that no significant amount of carbon precipitation to the sample surface has occurred upon natural cooling. This lack of additional carbon signal in the XPS data implies that the small increases in $I(G)$ and $I(D)/I(G)$ ratio seen in the in situ Raman data upon cooling (Figure 4c,d) do not relate to significant global precipitation of graphitic material to the sample surface. Instead, given the surface sensitivity of XPS compared to the more bulk-sensitive Raman spectroscopy,[20] it is suggested that upon natural cooling a small amount of deleterious carbon precipitates from the oversaturated Ni(-C) particles but remains localized at the direct Ni(-C)/carbon matrix interface while the surface of the nanocomposite films is not strongly modified by carbon precipitation upon cooling. The conclusion that the amount of carbon precipitation is small is also corroborated by the preservation of the comparatively high Ni(-C) signal in the cooled films (853.4 eV Ni 2p/283.7

eV C 1s) which implies that after natural cooling a significant amount of carbon is still interstitially dissolved in the Ni(-C) crystallites. This is also in good agreement with the comparably high carbon content of 0.19 ± 0.07 atom % in the Ni after natural cooling, as estimated from the in situ XRD data above.

■ DISCUSSION

Evolution of Nickel (Carbide)/Carbon Nanocomposites. Based on our experimental results we now present a coherent model of thermally induced effects on metastable Ni carbide/a-C nanocomposites and contextualize the findings with respect to prior literature. See Figure 6 for a schematic illustration of the salient stages of this model.

Our as-deposited films show a structure of columnar metastable Ni_3C crystals embedded in an a-C matrix. This morphology and its metastable nature are related to an interplay of repeated nucleation events and the dominance of surface diffusion effects during the nonequilibrium sputter deposition at room temperature, where bulk diffusion is considered to be negligible during film deposition.[22,31,97] During the postdeposition heating studied here, the metastable system moves toward thermal equilibrium at elevated temperatures which enables several reaction pathways to become activated, including bulk-diffusion related mechanisms.

First, the as-deposited metastable Ni_3C nanocrystallites in the a-C matrix isothermally decompose with a reaction onset temperature of ∼300 °C, whereby metallic fcc Ni with interstitially dissolved carbon (Ni(−C)) is formed. At 300 °C the Ni(−C) is however oversaturated with carbon as the initial carbon content of Ni_3C is 25 atom % while fcc Ni at 300 °C has a maximum carbon solubility of ∼0.01 atom %.[32,80] Thus, concurrent to the Ni_3C to fcc Ni(-C) transformation, carbon is partially expelled by diffusion from the Ni(-C) particles due to the strong carbon oversaturation. At a low temperature of 300 °C, we find that the expelled carbon cannot, however, rearrange into graphitic domains over the time scales considered but instead adds to the already present amorphous carbon matrix. This is consistent with recent ex situ work on decomposition and carbon shell formation for isolated, pure Ni_3C nanocrystals.[35,65,98] Thus, the overall isothermal Ni_3C decomposition at 300 °C may be described by the two concurrent processes of a solid state phase transition coupled with a partial phase separation:

$$Ni_3C \xrightarrow{300\,°C} fcc\ Ni(-C_{x+y})$$

$$fcc\ Ni(-C_{x+y}) \xrightarrow{300\,°C} fcc\ Ni(-C_x) + y\,a\text{-}C$$
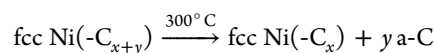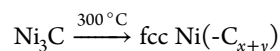
where Ni(-C) symbolizes a solid solution of carbon in fcc Ni. The expelled y a-C adds to the already initially present a-C matrix. Exact values for x and y remain unknown.

Concomitant grain growth of the Ni-based filler crystallites is observed to be very limited at 300 °C at the time scales considered. Therefore, annealing at 300 °C leaves the overall morphology of the nanocomposite thin films largely unchanged while only changing the crystallographic phase of the filler material. This shows that phase transformations and film morphology modifications can be decoupled in metastable nanocomposite films, which is highly desirable from a manufacturing perspective: For instance, our findings suggest that magnetic properties of the nanocomposites could be controlled without modification of the nanocomposite morphology since fcc Ni is ferromagnetic or superparamagnetic

depending on particle size while Ni_3C is in principle nonferromagnetic.[12,21,99]

Comparing to the wider literature, our observed decomposition of the a-C embedded Ni_3C nanocrystallites at 300 °C on a tens of minutes time scale is faster than previously reported hour-long conversion processes at ∼300 °C for pure Ni_3C crystallites.[65,100,101] It is also lower in temperature compared to other reports which observed >400 °C decomposition temperatures for pure isolated Ni_3C crystals.[35,102] This may be related to a lower degree of order in our sputter-deposited Ni_3C crystals,[103] in particular in terms of the degree of order in the carbon sublattice within the hcp Ni parent phase. Thus, the state of the as-deposited Ni carbide used here may also be described as the recently suggested Ni carbide form hcp NiC_y, which is comprised of a hcp Ni sublattice and a somewhat disordered interstitial carbon sublattice.[24] (See also the Supporting Information for a comment on Ni_3C assignment/definition used here.[24,64−66]) We note that this could be a generic feature of similarly sputter-deposited nickel carbide/a-C nanocomposites, where commonly nickel carbide decomposition temperatures of around 300−400 °C are reported.[6,12,13,28] The observed time dependence of isothermal decomposition at 300 °C for our films (inset in Figure 3b) can be fitted with the semiempirical Johnson−Mehl−Avrami−Kolmogorov (JMAK) equation,[104] wherefrom we estimate a maximum reaction rate[105] of $r_{max} = 1/t_{0.5} \sim$ 0.12%/s at 300 °C and an Avrami exponent n in the range 2.5−4.1. The physical meaning of Avrami exponents for systems with complex concurrent reactions as in our system, where a solid state transition ($Ni_3C \rightarrow fcc\ Ni(-C_{x+y})$) is coupled with a phase separation (fcc $Ni(-C_{x+y}) \rightarrow fcc\ Ni(-C_x) + y$ a-C)), remains however under debate and Avrami coefficients alone are therefore normally not sufficient to robustly determine microscopic nucleation and growth mechanics.[104]

While annealing at 300 °C is sufficient to transform the initially present Ni_3C nanocrystallites into fcc Ni(-C), only when the temperature is further increased (stepwise up to 800 °C) do two further major processes become thermally activated: (1) a-C graphitization and (2) Ni grain growth and phase separation.

In the first process the a-C in the matrix (including the expelled carbon from the Ni_3C decomposition) starts to graphitize into extended sp^2-bonded regions ("nanocrystalline graphite"). Since direct, noncatalyzed a-C → graphitic carbon reactions are known to be negligible in the considered temperature region of 300−800 °C,[31] the observed isothermal graphitization during heating from 400 to 700 °C suggests catalytic involvement of the Ni(-C) filler particles. As carbon solubility in fcc Ni increases with temperature,[32] the observed graphitization is indicative of a dynamic Ni-bulk-mediated process in which carbon species from the a-C surroundings are taken up into the Ni(-C) particles upon increasing annealing temperature and subsequently nucleate as graphitic carbon while segregating from the Ni(-C) at temperature.[70,106] Our in situ Raman data (Figure 4b) confirms that this Ni-catalyzed graphitization of the a-C matrix occurs upon heating and isothermal annealing. The reaction may be symbolized by

$$a\text{-}C \xrightarrow{Ni(-C),\,400-800\,°C} graphitic\ carbon$$
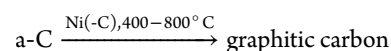
This resembles metal-induced-crystallization (MIC) phenomena in diverse materials systems such as metal−carbon,[73,107] metal−Si,[108] and metal−Ge.[109] It is also

reminiscent of carbon nanotube and graphene growth from gaseous[88,110,111] and solid state carbon[72–74] sources, where also Ni-bulk- or Ni-subsurface-mediated graphitization has been suggested as a major mechanism.[74,88,110,111] A significant difference from other MIC systems, however, is that in the present Ni–carbon nanocomposites the Ni-based crystallites are highly saturated with carbon *at all stages* of processing (including the as-deposited metastable Ni_3C state) and MIC can quickly proceed when thermally activated without the requirement of further carbon take-up, while in other MIC systems typically major constituent dissolution has to precede the stages of supersaturation and crystallization onset.

Upon further increasing the annealing temperature in the range 400−800 °C, the resulting sp^2-bonded graphitic regions increase in crystallite size forming nanocrystalline graphite with grain sizes of ∼60 nm. In contrast, in prior literature Ni has been shown to catalyze a-C to form high quality graphitic layers with micrometer lateral extents[72] and has even been demonstrated to produce high-quality monolayer graphene during heating at ∼600 °C when carbon feeding is kinetically controlled to suitably low levels.[74] To explain the comparably poor crystallite size of the graphitic material formed in our films, the kinetic aspects of the nanocomposite system evolution have to be considered: In the nanocomposite films examined here the overall carbon content is ∼70 atom %, which is significantly above the maximum carbon solubility in Ni *at all stages* of processing up to 800 °C (maximum carbon solubility in Ni at 800 °C is ∼0.5 atom %[32,80]). Therefore, the Ni crystallites in our experiments are at all stages strongly overfed with carbon both from the already interstitially dissolved carbon and from the surrounding carbon matrix. The correspondingly high carbon arrival rates to the catalytically active Ni(-C) in turn impede formation of large area graphitic domains, as the graphite nucleation rates are too high and the resulting time scales are insufficient to heal out defects. Instead the high carbon content of the Ni(-C) particles throughout processing results in the observed nanocrystalline graphite formation in the carbon matrix. This situation is analogous to catalyst poisoning or coking mechanisms in classical heterogeneous catalysis.[112] We emphasize that this highly bulk supersaturated nature at all processing stages and the intrinsically high carbon arrival rates from the surroundings are hallmark features of the thermal evolution mechanism in such metal/carbon nanocomposites, which clearly separates this class of materials from other metal−carbon systems where carbon influx to the interface can be controlled at lower rates, such as in balanced heterogeneous catalysis reactions[112,113] or graphene[35−42] and CNT[45−59] growth from Ni catalysts.

The second process concurrent to a-C graphitization is grain growth in the Ni(-C) crystallites, which upon higher annealing temperatures destroys the fine nanometer-scale columnar grain structure of the nanocomposite films. Connected with the Ni(-C) grain growth, the Ni(-C) particles and nanocrystalline graphite regions phase separate into a coarse film morphology for annealing up to 800 °C. This is consistent with previous studies of such nanocomposite systems.[6,31] It is interesting to note that compared to the ex situ studied Co−C and Cu−C systems in ref 31, where upon phase separation the metal layer formed on top of the carbon layer, we find in our experiments the formation of a nanocrystalline graphite layer roughly on top of a Ni layer (Figure 1a). As suggested above, Ni-bulk-mediated diffusion effects are highly important for higher temperature annealing in our nanocomposites. In fact, we suggest that

carbon diffusion through the bulk of the Ni(-C) particles links the above-described graphitization mechanism with the Ni grain growth and Ni−carbon phase separation. The main reason for this link is the comparably negligible self-diffusivity of carbon in amorphous carbon[31] which results in the Ni particles being the primary pathway for any possible carbon rearrangement. Throughout this carbon rearrangement process the Ni particles, however, do not remain statically embedded in the mobile, graphitizing carbon matrix but instead undergo grain growth and become mobile themselves. Previous TEM studies of Ni nanocrystals on a-C films also support a strong link between increasing Ni crystal mobility/reshaping and a-C graphitization.[69,70] Thus, we identify dynamic uptake and loss of carbon from/into the carbon matrix as a major governing factor for Ni(-C) particle evolution, where again the very high carbon content at all stages of processing is a distinctive feature of metal−carbon nanocomposite thin film systems such as ours.

Upon natural cooling the film morphologies are largely preserved, even when cooling from high temperature. Despite a significant decrease in thermodynamically predicted carbon solubility (0.5 atom % at 800 °C to <0.01 atom % at room temperature[32,80]) in the Ni(-C) particles upon cooling, we find from in situ XPS and XRD only limited signs of actual carbon precipitation upon cooling and instead find that still significant amounts of carbon remain dissolved interstitially in the Ni crystallites even after cooling. The estimated carbon content from in situ XRD after cooling from 800 °C to room temperature was 0.19 ± 0.07 atom % in the Ni, which would correspond to the expected equilibrium carbon content in Ni for temperatures between 580 and 690 °C.[80] The process upon cooling may thus be described as

$$\text{fcc Ni(-}C_{a+b}) \xrightarrow{\text{cool}} \text{fcc Ni(-}C_a) + b\,\text{a-C} \qquad \text{with } a \gg b$$
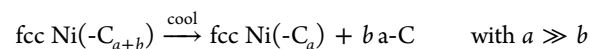
We suggest that two factors hinder extensive carbon precipitation out of the Ni at natural cooling rates in our experiments: First, the concentration-gradient-driven diffusion of carbon out of the Ni(-C) is small since outward carbon diffusion is directed toward the interface to a fully carbon saturated matrix (nanocrystalline graphite in matrix). This is a generic feature of two-phase nanocomposite thin films which show small but finite miscibility. Second, the diffusivity of carbon in Ni(-C) is comparatively slow in transporting significant carbon out of the Ni(-C) toward the Ni(-C)/nanocrystalline graphite interface for the cooling rates used here.[110,114] Upon reaching this interface, then the almost negligible self-diffusivity of carbon in a-C or graphite[31] hinders onward carbon transport, thus locking precipitated carbon at the Ni(-C) interface. Combined, these factors prohibit significant carbon precipitation from the Ni crystallites to the sample surface upon natural cooling, and thus allow nanocomposite structure engineering predominantly based on the selection of the heating rate and treatment temperature instead of technically more demanding cooling rate selection via, e.g., controlled quenching.

Overall, the structural and morphological nanocomposite evolution during annealing that is observed in situ here is consistent with recent ex situ work on Ni (carbide)/a-C films[28] and on Co (carbide)/a-C nanocomposites,[31] where similarly low temperature carbide disintegration and higher temperature graphitization and phase separation were inferred from ex situ measurements. This emphasizes the generic nature of our in situ findings. While the films studied here were deposited at

nonequilibrium conditions at room temperature, we note that the here observed mechanisms are also relevant for nanocomposite sputter deposition at elevated temperatures (i.e., with intentional substrate heating), where nonequilibrium effects[22,31,97] from the deposition process and thermally induced processes are active in parallel. This conclusion is consistent with the previously reported properties of Ni–carbon nanocomposites that were sputter deposited at increasingly elevated deposition temperatures.[14,15,17–21,26]

Ni₃C as a Possible Graphene/CNT Growth Catalyst. Beyond its application as a functional coating, metastable Ni₃C has also been recently discussed as an intermediate catalyst phase in graphene[35–44] synthesis via CVD and solid-state growth as well as in CNT CVD.[45–60] To date, there is however a lack of in situ studies with Ni₃C to directly elucidate the metastable carbide's role in graphene and CNT growth. Therefore, our findings here may also serve as a first approximate model system analogue for graphene and CNT growth from Ni₃C catalysts.

Typical temperatures for CVD and solid state growth of graphene and CNTs range from 450 to 1000 °C. Thus, the fast decomposition of Ni₃C observed here at temperatures as low as 300 °C suggests that it is unlikely that a crystalline bulk Ni₃C carbide is involved in Ni-catalyzed graphitic nanostructure growth under typical graphene and CNT growth conditions, especially for typical growth temperatures above 300 °C and common holding/growth times in the range of minutes. Our in situ observations thereby experimentally reaffirm recent theoretical work that similarly suggests that crystalline bulk Ni₃C is unlikely to directly partake in graphene formation because, as here, crystalline Ni₃C was found to decompose already prior to extended growth of graphitic material.[39] In turn, our results suggest that, in the higher temperature range typically used (>300 °C), it is not bulk Ni₃C but rather Ni₃C's decomposition product, a solid solution of carbon in fcc Ni (Ni(-C)), which is the active graphene and CNT growth catalyst phase. This is in excellent agreement with previous in situ studies on CVD[88,110,115] and solid state growth[74] of graphene from Ni catalysts that have excluded the formation of a structural Ni₃C *bulk* carbide during graphene formation (while a monolayer thin Ni₂C carbide surface reconstruction can partake under certain low temperature graphene growth conditions[91]). Our observations here now suggest that, even when crystalline bulk Ni₃C is the starting catalyst material in graphene or CNT growth, the facile thermal decomposition of bulk Ni₃C toward Ni(-C) precedes the graphitization of carbon, thus resulting in Ni(-C) being the actual active catalyst bulk phase of graphene and CNT growth under typical conditions. Exceptions may include growth conditions with exceptionally high heating rates[37,41] or nonequilibrium conditions where, e.g., Ni precursors are continuously fed during the graphitic material growth.[59] This is in contrast to catalysts which are comparably stronger carbide formers (such as Fe) where thermodynamically stable carbide bulk phases can readily partake in carbon nanostructure growth.[76,78]

CONCLUSIONS

In summary, we employed complementary in situ characterization to identify key factors governing thermally induced phase transitions in metastable Ni₃C/a-C nanocomposites. At low temperature (300 °C) isothermal decomposition of the Ni₃C filler phase into fcc Ni(-C) and a-C occurs, where the released carbon further adds to the carbon matrix. The finely

nanoscaled morphology of the composites remains however preserved at the low annealing temperature. In contrast, isothermal Ni-catalyzed graphitization of the amorphous carbon matrix and a linked bulk-diffusion-mediated phase separation into coarse Ni and nanocrystalline graphite grains sets in only at higher temperatures (400–800 °C). This shows that filler phase transformations and nanocomposite morphology modifications can be decoupled upon thermal postdeposition processing which is technologically advantageous. Precipitation of additional carbon from the Ni upon cooling was found to be minor for natural cooling rates. Our findings suggest that the high carbon content of the Ni filler crystallites at all stages of processing is the key property of such metal (carbide)/carbon nanocomposites that determines their thermal evolution. In the wider context of the recently much debated role of Ni₃C as a graphene and CNT growth catalyst, the low stability of Ni₃C directly observed here suggests that it is not bulk Ni₃C but fcc Ni(-C) that is the active bulk catalyst phase under typical graphene/CNT growth conditions.

ASSOCIATED CONTENT

Ⓢ Supporting Information

The Supporting Information is available free of charge on the ACS Publications website at DOI: 10.1021/acs.jpcc.6b01555.

> Detailed experimental methods description; comments on estimation of temperatures and Ni₃C phase definition/assignment; table of XPS BE assignments (PDF)

AUTHOR INFORMATION

Corresponding Author
*E-mail: bernhard.bayer@univie.ac.at. Tel.: +43-1-4277-72870.
Notes
The authors declare no competing financial interest.

ACKNOWLEDGMENTS

REFERENCES

(1) Ajayan, P. M.; Schadler, L. S.; Braun, P. V. *Nanocomposite Science and Technology*; John Wiley & Sons: 2006.

(2) Dimigen, H.; Hübsch, H.; Memming, R. Tribological and Electrical Properties of Metal-containing Hydrogenated Carbon Films. *Appl. Phys. Lett.* **1987**, *50*, 1056−1058.

(3) Kot, M.; Major, Ł.; Chronowska-Przywara, K.; Lackner, J.; Waldhauser, W.; Rakowski, W. The Advantages of Incorporating CrxC Nanograins into an aC: H Matrix in Tribological Coatings. *Mater. Eng.* **2014**, *56*, 981−989.

(4) Fonseca, F.; Ferlauto, A.; Alvarez, F.; Goya, G.; Jardim, R. Morphological and Magnetic Properties of Carbon−nickel Nano-composite Thin Films. *J. Appl. Phys.* **2005**, *97*, 044313.

(5) Pisana, S.; Mosendz, O.; Parker, G.; Reiner, J.; Santos, T.; McCallum, A.; Richter, H.; Weller, D. Effects of Grain Microstructure on Magnetic Properties in FePtAg-C Media for Heat Assisted Magnetic Recording. *J. Appl. Phys.* **2013**, *113*, 043910.

(6) Koppert, R.; Uhlig, S.; Schmid-Engel, H.; Göttel, D.; Probst, A.-C.; Schultes, G.; Werner, U. Structural and Physical Properties of Highly Piezoresistive Nickel Containing Hydrogenated Carbon Thin Films. *Diamond Relat. Mater.* **2012**, *25*, 50−58.

(7) Hong, Z.-C.; Shiue, S.-T. Effects of Annealing Temperature on Characteristics of Amorphous Nickel Carbon Thin Film Alloys Deposited on N-Type Silicon Substrates by Reactive Sputtering. *Thin Solid Films* **2016**, DOI: 10.1016/j.tsf.2016.04.032.

(8) Haslam, G. E.; Chin, X.-Y.; Burstein, G. T. Passivity and Electrocatalysis of Nanostructured Nickel Encapsulated in Carbon. *Phys. Chem. Chem. Phys.* **2011**, *13*, 12968−12974.

(9) Ingham, B.; Gaston, N.; Fahy, K.; Chin, X. Y.; Dotzler, C. J.; Rees, E.; Haslam, G.; Barber, Z. H.; Burstein, G. T.; Ryan, M. P. Extended X-Ray Absorption Fine Structure and X-Ray Diffraction Examination of Sputtered Nickel Carbon Binary Thin Films for Fuel Cell Applications. *J. Phys. Chem. C* **2012**, *116*, 6159−6165.

(10) Bettini, L. G.; Divitini, G.; Ducati, C.; Milani, P.; Piseri, P. Nickel Nanoparticles Effect on the Electrochemical Energy Storage Properties of Carbon Nanocomposite Films. *Nanotechnology* **2014**, *25*, 435401.

(11) Jansson, U.; Lewin, E. Sputter Deposition of Transition-Metal Carbide films—A Critical Review from a Chemical Perspective. *Thin Solid Films* **2013**, *536*, 1−24.

(12) Mamezaki, O.; Adachi, H.; Tomita, S.; Fujii, M.; Hayashi, S. Thin Films of Carbon Nanocapsules and Onion-like Graphitic Particles Prepared by the Cosputtering Method. *Jpn. J. Appl. Phys.* **2000**, *39*, 6680.

(13) Shi, J.; Hashiba, Y.; Nittono, O. Preparation and Character-ization of Ni-C Composite Films. *J. Mater. Sci.* **2001**, *36*, 343−349.

(14) Kovács, G. J.; Sáfrán, G.; Geszti, O.; Ujvári, T.; Bertóti, I.; Radnóczi, G. Structure and Mechanical Properties of Carbon−nickel and CNx−nickel Nanocomposite Films. *Surf. Coat. Technol.* **2004**, *180*, 331−334.

(15) Sedláčková, K.; Lobotka, P.; Vávra, I.; Radnóczi, G. Structural, Electrical and Magnetic Properties of Carbon−nickel Composite Thin Films. *Carbon* **2005**, *43*, 2192−2198.

(16) Kukiełka, S.; Gulbiński, W.; Pauleau, Y.; Dub, S.; Grob, J. Composition, Mechanical Properties and Friction Behavior of Nickel/hydrogenated Amorphous Carbon Composite Films. *Surf. Coat. Technol.* **2006**, *200*, 6258−6262.

(17) Sedláčková, K.; Czigany, Z.; Ujvari, T.; Bertoti, I.; Grasin, R.; Kovacs, G. J.; Radnoczi, G. The Effect of the Carbon Matrix on the Mechanical Properties of Nanocomposite Films Containing Nickel Nanoparticles. *Nanotechnology* **2007**, *18*, 445604.

(18) Kovács, G. J.; Veres, M.; Koós, M.; Radnóczi, G. Raman Spectroscopic Study of Magnetron Sputtered Carbon−nickel and Carbon Nitride−nickel Composite Films: The Effect of Nickel on the Atomic Structure of the C/CNx Matrix. *Thin Solid Films* **2008**, *516*, 7910−7915.

(19) Kovács, G. J.; Bertóti, I.; Radnóczi, G. X-Ray Photoelectron Spectroscopic Study of Magnetron Sputtered Carbon−nickel Composite Films. *Thin Solid Films* **2008**, *516*, 7942−7946.

(20) Abrasonis, G.; Krause, M.; Mücklich, A.; Sedlackova, K.; Radnóczi, G.; Kreissig, U.; Kolitsch, A.; Möller, W. Growth Regimes and Metal Enhanced 6-Fold Ring Clustering of Carbon in Carbon−nickel Composite Thin Films. *Carbon* **2007**, *45*, 2995−3006.

(21) Abrasonis, G.; Scheinost, A. C.; Zhou, S.; Torres, R.; Gago, R.; Jiménez, I.; Kuepper, K.; Potzger, K.; Krause, M.; Kolitsch, A.; et al. X-Ray Spectroscopic and Magnetic Investigation of C:Ni Nano-composite Films Grown by Ion Beam Cosputtering. *J. Phys. Chem. C* **2008**, *112*, 12628−12637.

(22) El Mel, A.; Bouts, N.; Grigore, E.; Gautron, E.; Granier, A.; Angleraud, B.; Tessier, P. Shape Control of Nickel Nanostructures Incorporated in Amorphous Carbon Films: From Globular Nano-particles toward Aligned Nanowires. *J. Appl. Phys.* **2012**, *111*, 114309.

(23) Bosworth, D. A.; Stelmashenko, N. A.; Barber, Z. H. Structural Control of Carbon Nickel Nano-Composite Thin Films without Substrate Heating. *Thin Solid Films* **2013**, *540*, 10−16.

(24) Furlan, A.; Lu, J.; Hultman, L.; Jansson, U.; Magnuson, M. Crystallization Characteristics and Chemical Bonding Properties of Nickel Carbide Thin Film Nanocomposites. *J. Phys.: Condens. Matter* **2014**, *26*, 415501.

(25) Kelling, J.; Zahn, P.; Schuster, J.; Gemming, S. Elastic and Piezoresistive Properties of Nickel Carbides from First-Principles. **2016**, arXiv:1604.00328 [cond-mat.mtrl-sci]. arXiv.org e-Print archive. https://arxiv.org/abs/1604.00328.

(26) Abrasonis, G.; Kovacs, G. J.; Ryves, L.; Krause, M.; Mücklich, A.; Munnik, F.; Oates, T.; Bilek, M.; Möller, W. Phase Separation in Carbon-Nickel Films during Hyperthermal Ion Deposition. *J. Appl. Phys.* **2009**, *105*, 083518.

(27) Abrasonis, G.; Kovács, G. J.; Tucker, M. D.; Heller, R.; Krause, M.; Guenette, M. C.; Munnik, F.; Lehmann, J.; Tadich, A.; Cowie, B. C. C.; et al. Sculpting Nanoscale Precipitation Patterns in Nano-composite Thin Films via Hyperthermal Ion Deposition. *Appl. Phys. Lett.* **2010**, *97*, 163108.

(28) El Mel, A.; Gautron, E.; Angleraud, B.; Granier, A.; Tessier, P. Synthesis of Nickel-Filled Carbon Nanotubes at 350° C. *Carbon* **2011**, *49*, 4595−4598.

(29) Krause, M.; Mücklich, A.; Oates, T. W.; Zschornak, M.; Wintz, S.; Endrino, J. L.; Baehtz, C.; Shalimov, A.; Gemming, S.; Abrasonis, G. Tilting of Carbon Encapsulated Metallic Nanocolumns in Carbon-Nickel Nanocomposite Films by Ion Beam Assisted Deposition. *Appl. Phys. Lett.* **2012**, *101*, 053112.

(30) Krause, M.; Buljan, M.; Mücklich, A.; Möller, W.; Fritzsche, M.; Facsko, S.; Heller, R.; Zschornak, M.; Wintz, S.; Endrino, J. L.; et al. Compositionally Modulated Ripples during Composite Film Growth: Three-Dimensional Pattern Formation at the Nanoscale. *Phys. Rev. B: Condens. Matter Mater. Phys.* **2014**, *89*, 085418.

(31) Berndt, M.; Abrasonis, G.; Kovács, G. J.; Krause, M.; Munnik, F.; Heller, R.; Kolitsch, A.; Möller, W. Bulk Diffusion Induced Structural Modifications of Carbon-Transition Metal Nanocomposite Films. *J. Appl. Phys.* **2011**, *109*, 063503.

(32) Singleton, M.; Nash, P. The C-Ni (Carbon-Nickel) System. *Bull. Alloy Phase Diagrams* **1989**, *10*, 121−126.

(33) Gibson, J. S.; Uddin, J.; Cundari, T. R.; Bodiford, N. K.; Wilson, A. K. First-Principle Study of Structure and Stability of Nickel Carbides. *J. Phys.: Condens. Matter* **2010**, *22*, 445503.

(34) Fang, C.; Sluiter, M.; Van Huis, M.; Zandbergen, H. Structural and Magnetic Properties of NiC X and NiN X (X= 0 to 1 3) Solid Solutions from First-Principles Calculations. *Phys. Rev. B: Condens. Matter Mater. Phys.* **2012**, *86*, 134114.

(35) Yoon, S.-M.; Choi, W. M.; Baik, H.; Shin, H.-J.; Song, I.; Kwon, M.-S.; Bae, J. J.; Kim, H.; Lee, Y. H.; Choi, J.-Y. Synthesis of Multilayer Graphene Balls by Carbon Segregation from Nickel Nanoparticles. *ACS Nano* **2012**, *6*, 6803−6811.

(36) Cao, Y.; Su, Q.; Che, R.; Du, G.; Xu, B. One-Step Chemical Vapor Synthesis of Ni/graphene Nanocomposites with Excellent Electromagnetic and Electrocatalytic Properties. *Synth. Met.* **2012**, *162*, 968−973.

(37) Xiong, W.; Zhou, Y. S.; Jiang, L. J.; Sarkar, A.; Mahjouri-Samani, M.; Xie, Z. Q.; Gao, Y.; Ianno, N. J.; Jiang, L.; Lu, Y. F. Single-Step Formation of Graphene on Dielectric Surfaces. *Adv. Mater.* **2013**, *25*, 630−634.

(38) Jiao, M.; Qian, H.; Page, A.; Li, K.; Wang, Y.; Wu, Z.; Irle, S.; Morokuma, K. Graphene Nucleation from Amorphous Nickel Carbides: QM/MD Studies on the Role of Subsurface Carbon Density. *J. Phys. Chem. C* **2014**, *118*, 11078−11084.

(39) Jiao, M.; Li, K.; Guan, W.; Wang, Y.; Wu, Z.; Page, A.; Morokuma, K. Crystalline Ni3C as Both Carbon Source and Catalyst for Graphene Nucleation: A QM/MD Study. *Sci. Rep.* **2015**, *5*, 12091.

(40) Son, I. H.; Song, H. J.; Kwon, S.; Bachmatiuk, A.; Lee, S. J.; Benayad, A.; Park, J. H.; Choi, J.-Y.; Chang, H.; Rümmeli, M. H. CO2 Enhanced Chemical Vapor Deposition Growth of Few-Layer Graphene over NiO X. *ACS Nano* **2014**, *8*, 9224−9232.

(41) Xiong, W.; Zhou, Y. S.; Hou, W. J.; Guillemet, T.; Silvain, J. F.; Gao, Y.; Lahaye, M.; Lebraud, E.; Xu, S.; Wang, X. W.; et al. Solid-State Graphene Formation via a Nickel Carbide Intermediate Phase. *RSC Adv.* **2015**, *5*, 99037−99043.

(42) Seah, C.-M.; Vigolo, B.; Chai, S.-P.; Ichikawa, S.; Gleize, J.; Le Normand, F.; Aweke, F.; Mohamed, A. R. Sequential Synthesis of Free-Standing High Quality Bilayer Graphene from Recycled Nickel Foil. *Carbon* **2016**, *96*, 268−275.

(43) Zhizhin, E.; Pudikov, D.; Rybkin, A.; Petukhov, A.; Zhukov, Y.; Shikin, A. Growth of Graphene Monolayer by "internal Solid-State Carbon Source": Electronic Structure, Morphology and Au Intercalation. *Mater. Des.* **2016**, *104*, 284−291.

(44) Chen, S.; Xiong, W.; Zhou, Y. S.; Lu, Y. F.; Zeng, X. C. An Ab Initio Study of the Nickel-Catalyzed Transformation of Amorphous Carbon into Graphene in Rapid Thermal Processing. *Nanoscale* **2016**, *8*, 9746−9755.

(45) Arie, T.; Nishijima, H.; Akita, S.; Nakayama, Y. Carbon-Nanotube Probe Equipped Magnetic Force Microscope. *J. Vac. Sci. Technol., B: Microelectron. Process. Phenom.* **2000**, *18*, 104−106.

(46) Ducati, C.; Alexandrou, I.; Chhowalla, M.; Robertson, J.; Amaratunga, G. The Role of the Catalytic Particle in the Growth of Carbon Nanotubes by Plasma Enhanced Chemical Vapor Deposition. *J. Appl. Phys.* **2004**, *95*, 6387−6391.

(47) Lin, M.; Ying Tan, J. P.; Boothroyd, C.; Loh, K. P.; Tok, E. S.; Foo, Y.-L. Direct Observation of Single-Walled Carbon Nanotube Growth at the Atomistic Scale. *Nano Lett.* **2006**, *6*, 449−452.

(48) Esconjauregui, S.; Whelan, C. M.; Maex, K. The Reasons Why Metals Catalyze the Nucleation and Growth of Carbon Nanotubes and Other Carbon Nanomorphologies. *Carbon* **2009**, *47*, 659−669.

(49) Rinaldi, A.; Abdullah, N.; Ali, M.; Furche, A.; Hamid, S. B. A.; Su, D. S.; Schlögl, R. Controlling the Yield and Structure of Carbon Nanofibers Grown on a Nickel/activated Carbon Catalyst. *Carbon* **2009**, *47*, 3023−3033.

(50) Sharma, R.; Chee, S.-W.; Herzing, A.; Miranda, R.; Rez, P. Evaluation of the Role of Au in Improving Catalytic Activity of Ni Nanoparticles for the Formation of One-Dimensional Carbon Nanostructures. *Nano Lett.* **2011**, *11*, 2464−2471.

(51) Pigos, E.; Penev, E. S.; Ribas, M. A.; Sharma, R.; Yakobson, B. I.; Harutyunyan, A. R. Carbon Nanotube Nucleation Driven by Catalyst Morphology Dynamics. *ACS Nano* **2011**, *5*, 10096−10101.

(52) Rinaldi, A.; Tessonnier, J.; Schuster, M. E.; Blume, R.; Girgsdies, F.; Zhang, Q.; Jacob, T.; Abd Hamid, S. B.; Su, D. S.; Schlögl, R. Dissolved Carbon Controls the Initial Stages of Nanocarbon Growth. *Angew. Chem., Int. Ed.* **2011**, *50*, 3313−3317.

(53) Panagiotopoulos, N. T.; Diamanti, E. K.; Koutsokeras, L. E.; Baikousi, M.; Kordatos, E.; Matikas, T. E.; Gournis, D.; Patsalas, P. Nanocomposite Catalysts Producing Durable, Super-Black Carbon Nanotube Systems: Applications in Solar Thermal Harvesting. *ACS Nano* **2012**, *6*, 10475−10485.

(54) Krause, M.; Haluška, M.; Abrasonis, G.; Gemming, S. SWCNT Growth from C: Ni Nanocomposites. *Phys. Status Solidi B* **2012**, *249*, 2357−2360.

(55) Mohammad, S. N. Unified Platform for the Chemical Reactivity and Catalytic Potential of Catalyst Nanoparticles of Even Very Diverse Structures and Characteristics for Nanotube (Including Carbon Nanotube) Syntheses. *J. Mater. Chem.* **2012**, *22*, 21560−21582.

(56) Achour, A.; El Mel, A.; Bouts, N.; Gautron, E.; Grigore, E.; Angleraud, B.; Le Brizoual, L.; Tessier, P.; Djouadi, M. Carbon Nanotube Growth at 420° C Using Nickel/carbon Composite Thin Films as Catalyst Supports. *Diamond Relat. Mater.* **2013**, *34*, 76−83.

(57) Yu, B.; Wang, S.; Zhang, Q.; He, Y.; Huang, H.; Zou, J. Ni3C-Assisted Growth of Carbon Nanofibres 300° C by Thermal CVD. *Nanotechnology* **2014**, *25*, 325602.

(58) Gómez-Gualdrón, D. A.; Beetge, J. M.; Balbuena, P. B. Characterization of Metal Nanocatalyst State and Morphology during Simulated Single-Walled Carbon Nanotube Growth. *J. Phys. Chem. C* **2013**, *117*, 12061−12070.

(59) Yu, B.; Zhang, Q.; Hou, L.; Wang, S.; Song, M.; He, Y.; Huang, H.; Zou, J. Temperature-Dependent Chemical State of the Nickel Catalyst for the Growth of Carbon Nanofibers. *Carbon* **2016**, *96*, 904−910.

(60) Melkhanova, S.; Haluska, M.; Hübner, R.; Kunze, T.; Keller, A.; Abrasonis, G.; Gemming, S.; Krause, M. Carbon: Nickel Nanocomposite Templates−predefined Stable Catalysts for Diameter-Controlled Growth of Single-Walled Carbon Nanotubes. *Nanoscale* **2016**, *8*, 14888−14897.

(61) Bayer, B. C.; Sanjabi, S.; Baehtz, C.; Wirth, C. T.; Esconjauregui, S.; Weatherup, R. S.; Barber, Z. H.; Hofmann, S.; Robertson, J. Carbon Nanotube Forest Growth on NiTi Shape Memory Alloy Thin Films for Thermal Actuation. *Thin Solid Films* **2011**, *519*, 6126−6129.

(62) Bayer, B. C.; Khan, A. F.; Mehmood, M.; Barber, Z. H. Effect of Substrate on Processing of Multi-Gun Sputter Deposited, near-Stoichiometric Ni2MnGa Thin Films. *Thin Solid Films* **2010**, *518*, 2659−2664.

(63) Gammer, C.; Mangler, C.; Rentenberger, C.; Karnthaler, H. Quantitative Local Profile Analysis of Nanomaterials by Electron Diffraction. *Scr. Mater.* **2010**, *63*, 312−315.

(64) Schaefer, Z. L.; Weeber, K. M.; Misra, R.; Schiffer, P.; Schaak, R. E. Bridging Hcp-Ni and Ni3C via a Ni3C1-X Solid Solution: Tunable Composition and Magnetism in Colloidal Nickel Carbide Nanoparticles. *Chem. Mater.* **2011**, *23*, 2475−2480.

(65) Chiang, R.-T.; Chiang, R.-K.; Shieu, F.-S. Emergence of Interstitial-Atom-Free HCP Nickel Phase during the Thermal Decomposition of Ni 3 C Nanoparticles. *RSC Adv.* **2014**, *4*, 19488−19494.

(66) Uhlig, S.; Struis, R.; Schmid-Engel, H.; Bock, J.; Probst, A.-C.; Freitag-Weber, O.; Zizak, I.; Chernikov, R.; Schultes, G. Piezoresistive Ni: aC: H Thin Films Containing Hcp-Ni or Ni 3 C Investigated by XRD, EXAFS, and Wavelet Analysis. *Diamond Relat. Mater.* **2013**, *34*, 25−35.

(67) Ferrari, A. C. Raman Spectroscopy of Graphene and Graphite: Disorder, Electron−phonon Coupling, Doping and Nonadiabatic Effects. *Solid State Commun.* **2007**, *143*, 47−57.

(68) Kidambi, P. R.; Bayer, B. C.; Weatherup, R. S.; Ochs, R.; Ducati, C.; Szabó, D. V.; Hofmann, S. Hafnia Nanoparticles−a Model System for Graphene Growth on a Dielectric. *Phys. Status Solidi RRL* **2011**, *5*, 341−343.

(69) Anton, R. On the Reaction Kinetics of Ni with Amorphous Carbon. *Carbon* **2008**, *46*, 656−662.

(70) Lamber, R.; Jaeger, N.; Schulz-Ekloff, G. Electron Microscopy Study of the Interaction of Ni, Pd and Pt with Carbon: I. Nickel Catalyzed Graphitization of Amorphous Carbon. *Surf. Sci.* **1988**, *197*, 402−414.

(71) Derbyshire, F.; Presland, A.; Trimm, D. Graphite Formation by the Dissolution—precipitation of Carbon in Cobalt, Nickel and Iron. *Carbon* **1975**, *13*, 111−113.

(72) Zheng, M.; Takei, K.; Hsia, B.; Fang, H.; Zhang, X.; Ferralis, N.; Ko, H.; Chueh, Y.-L.; Zhang, Y.; Maboudian, R.; et al. Metal-Catalyzed Crystallization of Amorphous Carbon to Graphene. *Appl. Phys. Lett.* **2010**, *96*, 063110.

(73) Saenger, K.; Tsang, J.; Bol, A.; Chu, J.; Grill, A.; Lavoie, C. In Situ X-Ray Diffraction Study of Graphitic Carbon Formed during Heating and Cooling of Amorphous-C/Ni Bilayers. *Appl. Phys. Lett.* **2010**, *96*, 153105.

(74) Weatherup, R. S.; Baehtz, C.; Dlubak, B.; Bayer, B. C.; Kidambi, P. R.; Blume, R.; Schloegl, R.; Hofmann, S. Introducing Carbon

Diffusion Barriers for Uniform, High-Quality Graphene Growth from Solid Sources. *Nano Lett.* **2013**, *13*, 4624−4631.

(75) Wenisch, R.; Hübner, R.; Munnik, F.; Melkhanova, S.; Gemming, S.; Abrasonis, G.; Krause, M. Nickel-Enhanced Graphitic Ordering of Carbon Ad-Atoms during Physical Vapor Deposition. *Carbon* **2016**, *100*, 656−663.

(76) Wirth, C. T.; Bayer, B. C.; Gamalski, A. D.; Esconjauregui, S.; Weatherup, R. S.; Ducati, C.; Baehtz, C.; Robertson, J.; Hofmann, S. The Phase of Iron Catalyst Nanoparticles during Carbon Nanotube Growth. *Chem. Mater.* **2012**, *24*, 4633−4640.

(77) Kidambi, P. R.; Blume, R.; Kling, J.; Wagner, J. B.; Baehtz, C.; Weatherup, R. S.; Schlögl, R.; Bayer, B. C.; Hofmann, S. In Situ Observations during Chemical Vapor Deposition of Hexagonal Boron Nitride on Polycrystalline Copper. *Chem. Mater.* **2014**, *26*, 6380−6392.

(78) Bayer, B. C.; Baehtz, C.; Kidambi, P. R.; Weatherup, R. S.; Mangler, C.; Kotakoski, J.; Goddard, C. J. L.; Caneva, S.; Cabrero-Vilatela, A.; Meyer, J. C.; et al. Nitrogen Controlled Iron Catalyst Phase during Carbon Nanotube Growth. *Appl. Phys. Lett.* **2014**, *105*, 143111.

(79) Caneva, S.; Weatherup, R. S.; Bayer, B. C.; Brennan, B.; Spencer, S. J.; Mingard, K.; Cabrero-Vilatela, A.; Baehtz, C.; Pollard, A. J.; Hofmann, S. Nucleation Control for Large, Single Crystalline Domains of Monolayer Hexagonal Boron Nitride via Si-Doped Fe Catalysts. *Nano Lett.* **2015**, *15*, 1867−1875.

(80) Natesan, K.; Kassner, T. Thermodynamics of Carbon in Nickel, Iron-Nickel and Iron-Chromium-Nickel Alloys. *Metall. Trans. A* **1973**, *4*, 2557−2566.

(81) Adelhelm, C.; Balden, M.; Rinke, M.; Stueber, M. Influence of Doping (Ti, V, Zr, W) and Annealing on the sp2 Carbon Structure of Amorphous Carbon Films. *J. Appl. Phys.* **2009**, *105*, 033522.

(82) Bock, M. C. D.; Denk, R.; Wirth, C. T.; Goldberg-Oppenheimer, P.; Hofmann, S.; Baumberg, J. J. Optical Feedback Mechanisms in Laser Induced Growth of Carbon Nanotube Forests. *Appl. Phys. Lett.* **2012**, *100*, 013112.

(83) Michaelis, F. B.; Weatherup, R. S.; Bayer, B. C.; Bock, M. C.; Sugime, H.; Caneva, S.; Robertson, J.; Baumberg, J. J.; Hofmann, S. Co-Catalytic Absorption Layers for Controlled Laser-Induced Chemical Vapor Deposition of Carbon Nanotubes. *ACS Appl. Mater. Interfaces* **2014**, *6*, 4025−4032.

(84) Pustovalov, V. K. Theoretical Study of Heating of Spherical Nanoparticle in Media by Short Laser Pulses. *Chem. Phys.* **2005**, *308*, 103−108.

(85) Bock, M. Optical Growth of Carbon Nanotubes. Ph.D. Thesis, University of Cambridge, Cambridge, U.K., 2012.

(86) Bayer, B. C.; Fouquet, M.; Blume, R.; Wirth, C. T.; Weatherup, R. S.; Ogata, K.; Knop-Gericke, A.; Schlögl, R.; Hofmann, S.; Robertson, J. Co-Catalytic Solid-State Reduction Applied to Carbon Nanotube Growth. *J. Phys. Chem. C* **2012**, *116*, 1107−1113.

(87) Bayer, B. C.; Castellarin-Cudia, C.; Blume, R.; Steiner, S. A.; Ducati, C.; Chu, D.; Goldoni, A.; Knop-Gericke, A.; Schlögl, R.; Cepek, C.; et al. Tantalum-Oxide Catalysed Chemical Vapour Deposition of Single- and Multi-Walled Carbon Nanotubes. *RSC Adv.* **2013**, *3*, 4086−4092.

(88) Weatherup, R. S.; Bayer, B. C.; Blume, R.; Ducati, C.; Baehtz, C.; Schlögl, R.; Hofmann, S. In Situ Characterization of Alloy Catalysts for Low-Temperature Graphene Growth. *Nano Lett.* **2011**, *11*, 4154−4160.

(89) Blume, R.; Rosenthal, D.; Tessonnier, J.-P.; Li, H.; Knop-Gericke, A.; Schlögl, R. Characterizing Graphitic Carbon with X-Ray Photoelectron Spectroscopy: A Step-by-Step Approach. *ChemCatChem* **2015**, *7*, 2871−2881.

(90) Goto, Y.; Taniguchi, K.; Omata, T.; Otsuka-Yao-Matsuo, S.; Ohashi, N.; Ueda, S.; Yoshikawa, H.; Yamashita, Y.; Oohashi, H.; Kobayashi, K. Formation of Ni3C Nanocrystals by Thermolysis of Nickel Acetylacetonate in Oleylamine: Characterization Using Hard X-Ray Photoelectron Spectroscopy. *Chem. Mater.* **2008**, *20*, 4156−4160.

(91) Patera, L. L.; Africh, C.; Weatherup, R. S.; Blume, R.; Bhardwaj, S.; Castellarin-Cudia, C.; Knop-Gericke, A.; Schloegl, R.; Comelli, G.;

Hofmann, S.; et al. In Situ Observations of the Atomistic Mechanisms of Ni Catalyzed Low Temperature Graphene Growth. *ACS Nano* **2013**, *7*, 7901−7912.

(92) Gelius, U.; Heden, P.; Hedman, J.; Lindberg, B.; Manne, R.; Nordberg, R.; Nordling, C.; Siegbahn, K. Molecular Spectroscopy by Means of ESCA III. Carbon Compounds. *Phys. Scr.* **1970**, *2*, 70.

(93) Kidambi, P. R.; Bayer, B. C.; Blume, R.; Wang, Z.-J.; Baehtz, C.; Weatherup, R. S.; Willinger, M.-G.; Schloegl, R.; Hofmann, S. Observing Graphene Grow: Catalyst−Graphene Interactions during Scalable Graphene Growth on Polycrystalline Copper. *Nano Lett.* **2013**, *13*, 4769−4778.

(94) Oswald, S.; Brückner, W. XPS Depth Profile Analysis of Non-stoichiometric NiO Films. *Surf. Interface Anal.* **2004**, *36*, 17−22.

(95) Weatherup, R. S.; D'Arsié, L.; Cabrero-Vilatela, A.; Caneva, S.; Blume, R.; Robertson, J.; Schloegl, R.; Hofmann, S. Long-Term Passivation of Strongly Interacting Metals with Single-Layer Graphene. *J. Am. Chem. Soc.* **2015**, *137*, 14358−14366.

(96) Blume, R.; Kidambi, P. R.; Bayer, B. C.; Weatherup, R. S.; Wang, Z.-J.; Weinberg, G.; Willinger, M.-G.; Greiner, M.; Hofmann, S.; Knop-Gericke, A.; et al. The Influence of Intercalated Oxygen on the Properties of Graphene on Polycrystalline Cu under Various Environmental Conditions. *Phys. Chem. Chem. Phys.* **2014**, *16*, 25989−26003.

(97) Petrov, I.; Barna, P.; Hultman, L.; Greene, J. Microstructural Evolution during Film Growth. *J. Vac. Sci. Technol., A* **2003**, *21*, S117−S128.

(98) Schaefer, Z. L.; Gross, M. L.; Hickner, M. A.; Schaak, R. E. Uniform Hollow Carbon Shells: Nanostructured Graphitic Supports for Improved Oxygen-Reduction Catalysis. *Angew. Chem.* **2010**, *122*, 7199−7202.

(99) Yue, L.; Sabiryanov, R.; Kirkpatrick, E.; Leslie-Pelecky, D. L. Magnetic Properties of Disordered Ni 3 C. *Phys. Rev. B: Condens. Matter Mater. Phys.* **2000**, *62*, 8969.

(100) Hofer, L.; Cohn, E.; Peebles, W. The Isothermal Decomposition of Nickel Carbide. *J. Phys. Colloid Chem.* **1950**, *54*, 1161−1169.

(101) Nagakura, S. Study of Metallic Carbides by Electron Diffraction Part I. Formation and Decomposition of Nickel Carbide. *J. Phys. Soc. Jpn.* **1957**, *12*, 482−494.

(102) Leng, Y.; Xie, L.; Liao, F.; Zheng, J.; Li, X. Kinetic and Thermodynamics Studies on the Decompositions of Ni 3 C in Different Atmospheres. *Thermochim. Acta* **2008**, *473*, 14−18.

(103) Sinharoy, S.; Smith, M.; Levenson, L. Thermal Decomposition of Nickel Carbide Thin Films. *Surf. Sci.* **1978**, *72*, 710−718.

(104) Ruitenberg, G.; Woldt, E.; Petford-Long, A. Comparing the Johnson−Mehl−Avrami−Kolmogorov Equations for Isothermal and Linear Heating Conditions. *Thermochim. Acta* **2001**, *378*, 97−105.

(105) Callister, W. D.; Rethwisch, D. G. *Materials Science and Engineering: An Introduction*; Wiley: New York, 2007; Vol. 7.

(106) Kling, J.; Hansen, T. W.; Wagner, J. B. Quantifying the Growth of Individual Graphene Layers by in Situ Environmental Transmission Electron Microscopy. *Carbon* **2016**, *99*, 261−266.

(107) Ramirez, A.; Itoh, T.; Sinclair, R. Crystallization of Amorphous Carbon Thin Films in the Presence of Magnetic Media. *J. Appl. Phys.* **1999**, *85*, 1508−1513.

(108) Nast, O.; Puzzer, T.; Koschier, L. M.; Sproul, A. B.; Wenham, S. R. Aluminum-Induced Crystallization of Amorphous Silicon on Glass Substrates above and below the Eutectic Temperature. *Appl. Phys. Lett.* **1998**, *73*, 3214−3216.

(109) Herd, S.; Chaudhari, P.; Brodsky, M. Metal Contact Induced Crystallization in Films of Amorphous Silicon and Germanium. *J. Non-Cryst. Solids* **1972**, *7*, 309−327.

(110) Weatherup, R. S.; Bayer, B. C.; Blume, R.; Baehtz, C.; Kidambi, P. R.; Fouquet, M.; Wirth, C. T.; Schlögl, R.; Hofmann, S. On the Mechanisms of Ni-Catalysed Graphene Chemical Vapour Deposition. *ChemPhysChem* **2012**, *13*, 2544−2549.

(111) Weatherup, R. S.; Dlubak, B.; Hofmann, S. Kinetic Control of Catalytic CVD for High-Quality Graphene at Low Temperatures. *ACS Nano* **2012**, *6*, 9996−10003.

(112) Trimm, D. Catalysts for the Control of Coking during Steam Reforming. *Catal. Today* **1999**, *49*, 3−10.

(113) Gonzalez, I.; De Jesus, J. C.; Cañizales, E.; Delgado, B.; Urbina, C. Comparison of the Surface State of Ni Nanoparticles Used for Methane Catalytic Decomposition. *J. Phys. Chem. C* **2012**, *116*, 21577−21587.

(114) Lander, J.; Kern, H.; Beach, A. Solubility and Diffusion Coefficient of Carbon in Nickel: Reaction Rates of Nickel-Carbon Alloys with Barium Oxide. *J. Appl. Phys.* **1952**, *23*, 1305−1309.

(115) Weatherup, R. S.; Amara, H.; Blume, R.; Dlubak, B.; Bayer, B. C.; Diarra, M.; Bahri, M.; Cabrero-Vilatela, A.; Caneva, S.; Kidambi, P. R.; et al. Interdependency of Subsurface Carbon Distribution and Graphene−Catalyst Interaction. *J. Am. Chem. Soc.* **2014**, *136*, 13698−13708.